Journal of Materials Chemistry A

Accepted Manuscript

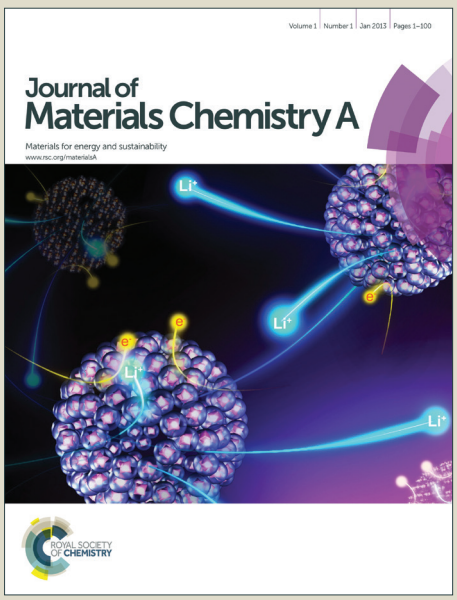

ROYAL SOCIETY OF CHEMISTRY

www.rsc.org/materialsA

Tailoring hierarchically structured SiO_2 spheres for high pressure CO_2 adsorption

Maximilian W. Hahn, Matthias Steib, Andreas Jentys*,

Johannes A. Lercher*

Technische Universität München, Department of Chemistry, Catalysis Research Center, Lichtenbergstraße 4, 85747 Garching, Germany

* Corresponding author. Phone +49-(89)-289-13540/13538. Fax: +49-(89)-289-13544.
Email: johannes.lercher@mytum.de, jentys@mytum.de

Abstract

The synthesis, characterization, and experimental validation of hierarchically structured, millimeter-sized SiO_2 spheres with high CO_2 uptake capacities has been systematically explored. The solvents employed during synthesis (aniline, benzyl alcohol and butanol) of the silica structures from alkoxisilanes strongly influence the physicochemical properties by controlling hydrolysis and condensation rates. The new sorbents possess specific surface areas up to 660 $m^2 \cdot g^{-1}$ and a hierarchically ordered mesoporous/macroporous pore structure. The SiO_2 spheres showed lower heats of adsorption of CO_2 (8–17 $kJ \cdot mol^{-1}$) compared to the benchmark zeolite 13X, facilitating the desorption of CO_2 in temperature swing adsorption applications. Moreover, the CO_2 adsorption isotherms of SiO_2 spheres are less steep compared to zeolite 13X resulting in an increased CO_2 uptake capacity in pressure swing adsorption processes. Addition of Zr^{4+} cations to SiO_2 increases the CO_2 uptake by generating Lewis acid-base sites. Because the presence of Zr^{4+} in the structure also dramatically enhances the abrasion resistance of the sorbents, additional coagulation steps, required for the benchmark sorbents, are not necessary.

Table of contents entry

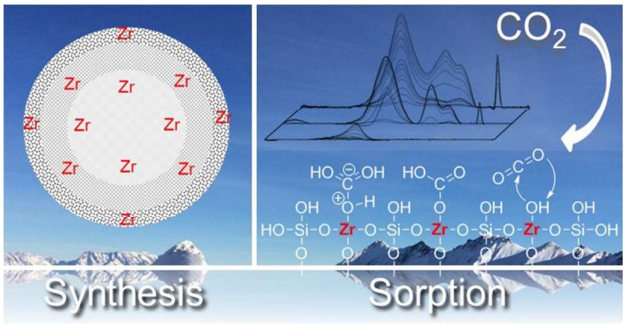

Mesoscopic sorbents are synthesized with various solvents for CO_2 capture at elevated pressure and modified with Zr^{4+} cations to increase the uptake performance.

1. Introduction

Fossil fuels, such as oil, gas, and coal, are the backbone of our energy consumption and will remain dominating far out into the future.[1, 2, 3] Investments in alternative energies such as wind and solar energy, as well as biomass-derived fuels, are crucial in the path to limit further growth of non-renewable energy resources.[4] However, the cost associated with the decentralized structure of renewable energy and the strong fluctuations in availability lead to significant challenges to steadily cover the high energy demand of industrialized countries.[2, 4] Decreasing costs of natural gas and the low societal acceptance of nuclear energy[5] have led combined to the renaissance of gas and coal as dominating fossil carbon sources, varying in importance as direct consequence of the local availability.[6]

Because the anthropogenic CO_2 concentration has increased over the last decades, it is deemed crucial to control and decrease the CO_2 emissions of existing and newly built energy infrastructure relying on fossil fuels.[7] The currently practiced separation of CO_2 from flue gas stream with a post-combustion amine wash decreases the effectiveness of a coal-fired power plant by 10-12 %.[8] Therefore, alternative, more effective processes are being explored that include flue gas separation directly in the process.[9] Exemplarily, pre-combustion and oxyfuel processes are high pressure and high temperature processes using a highly enriched oxygen stream from which CO_2 has to be separated from H_2 (pre-combustion) or H_2O (oxyfuel).[9, 10] Implementation of such process not only requires new reactor engineering approaches, but also the development of cost effective adsorbents, well-adjusted to the new separation conditions.[11]

Adsorbents for pre-combustion are currently intensely investigated.[11-15] Exemplarily, Schell et al. investigated the adsorption equilibrium of CO_2 and H_2 on MCM-41 and metal organic framework (MOF) USO-2-Ni at different temperatures up to 140 °C and at pressures up to 150 bar.[14] However, the time-intensive synthesis in combination with high costs is a major drawback of these materials (MCM-41, SBA-15 and MOF).[16-19] This is related with the fact that the synthesis of the materials and the forming step are separated requiring several preparation steps. In contrast, emulsion based, biphasic chemistry allows to control the shape and meso-structure during material synthesis in one step.[20] Huo et al. synthesized mesoporous SiO_2 spheres synthesized similar to MCM-41 with a diameter of 0.5 - 1 mm in a one-step

procedure.[21] These SiO_2 spheres exhibited 2 nm pores and specific surface areas up to 1100 $m^2 \cdot g^{-1}$.[21] Nevertheless, the pore volumes of the SiO_2 spheres were only in the range of 0.24 – 0.54 $ml \cdot g^{-1}$ limiting the maximum CO_2 storage capacity. The larger, hierarchically structured, millimeter sized SiO_2 spheres (in the range of 1-2 mm), which were recently developed as sorbents and catalyst supports offer advantages compared to the former materials with respect to pore volume and pore size distribution.[22-25] The surface of the SiO_2 spheres is dominated by large pores allowing fast access of CO_2 from the gas phase into the sorbent, followed by a mesoporous inner part enabling high CO_2 sorption capacities (Figure 1).[23, 25] The sorption process of these materials was found to be not kinetically limited due to fast transport in the mesopores and relatively small domains of microporous SiO_2. It should be noted that with increasing pressure, the regime changes from Knudsen to bulk diffusion and therefore film diffusion is assumed to be the rate determining step, if transport limitations occur. High specific surface areas and well-ordered pore structures make the hierarchically structured SiO_2 spheres a promising alternative to zeolites, mesoporous silicates and MOFs for high pressure pre-combustion applications.

In this study, we investigate the influence of three solvents (aniline, benzyl alcohol, and butanol) with comparable density on the morphology of mesoscopic, hierarchically structured SiO_2 spheres for pre-combustion CO_2 separation. The difference in polarity of the solvents influenced the rate of hydrolysis, whereas the different basicity of the solvents directly affected the condensation reactions in the sol-gel process (Scheme 1). In part of the samples, Zr^{4+} cations were incorporated in the SiO_2 framework to enhance the interaction with CO_2 and increase separation from H_2. The uptake of CO_2 and N_2 (selected instead of H_2 as a non-explosive probe molecule) was investigated up to a pressure of 40 bar at two different temperatures. Thermodynamic parameters (ΔH^0_{ads}, ΔS^0_{ads}) were calculated using the Langmuir adsorption model. The structural and physicochemical properties of the adsorbents were investigated to derive structure activity relationships.

2. Experimental

2.1 Sorbent preparation and synthesis

SiO_2 spheres were synthesized according to Scholz et al. in a base catalyzed condensation reaction.[23, 25] Phenyltrimethoxysilane (PTMS, purity ≥ 97%), N-[3-(trimethoxysilyl)propyl]ethylendiamine (AAMS, purity ≥ 97%), zirconium(IV) *t*-butoxide (80 wt.% in 1-butanol), aniline (purity ≥ 99.5%), benzyl alcohol (purity ≥ 99%) and 2-butanol (anhydrous, purity ≥ 99.5%) were purchased from Sigma Aldrich. Tetraethylorthosilicate (TEOS) and the copolymer Pluronic® RPE 1740 were provided by WACKER and BASF, respectively. All chemicals were used without any further purification. Deionized water was the reaction medium in the reactor column.

The surfactant containing precursor solution was prepared by mixing 6.50 g of the surfactant Pluronic® RPE 1740 and 7.11 g of the solvent (aniline, benzyl alcohol or 2-butanol). 0, 5 and 25 wt.% of zirconium(IV) *t*-butoxide based on the amount of TEOS were added to the structure directing precursor solution. The addition of zirconium(IV) *t*-butoxide reduced the amount of solvent accordingly. The Si precursor rich solution contained 7.20 g TEOS, 4.01 g AAMS and 5.18 g of PTMS. Both solutions were stirred separately for 15 min. Prior to injection, the two solutions were merged and mixed for additional 10 min. The pH of the final precursor emulsion was measured with a Mettler Toledo Seven CompactTM pH/ion meter S220 with a LoT 403-M8-S7/120 electrode. The design and operation conditions of the reactor column are described in the supporting information (Figure S 1). The spheres were directly formed by micelle formation and base catalyzed condensation. The particle size of the SiO_2 spheres was perfectly spherical and mainly influenced by the injection rate of the mixed precursor solution and the bypass stream in the reactor column. After removing the SiO_2 spheres at the bottom of the column, they were washed three times with copious amount of deionized water. The SiO_2 spheres were aged in deionized water overnight under ambient conditions in order to assure full condensation of the spheres. Afterwards, the SiO_2 spheres were washed with 3 × 30 mL of water and 3 × 30 mL of ethanol, then dried overnight. All adsorbents in this work were calcined in synthetic air (100 mL·min^{-1}) at 600 °C for 3 h with a

heating rate of 1 °C·min^{-1} to ensure the removal of all remaining surfactants. SBA-15 was synthesized according to literature.[16, 26]

2.2 Sorbent characterization

The C, H and N contents of SiO_2 spheres were determined by combustion analysis. The Zr^{4+} content of the sorbents was determined with inductively coupled plasma optical emission spectrometry (ICP OES). The detailed procedure of each method is described in the supporting information.

SEM images were recorded with a Jeol JSM 7500F microscope. Images were taken with a resolution from 1 µm to 100 µm with a lower electron image (LEI) and a yttrium aluminum garnet (YAG) detector. Sputter coating was not performed on all samples.

A Philips X'pert diffractometer equipped with an X'celerator module, using Cu Kα radiation, was used to measure powder X-ray diffraction (XRD) patterns. Diffractograms were obtained from $2\Theta = 5°$ to $40°$ with a step size of 0.033°.

The surface area, micro- and mesopore volume, as well as the according pore size distribution were determined by nitrogen physisorption at -196 °C using a QUADRASORB SI automated surface area and pore size analyzer. Prior to analysis, samples were evacuated at 200 °C for 3 h using a Quantachrome FloVac degasser. Surface area was determined using the Brunauer-Emmett-Teller (BET) method. Pore volumes were divided into micropores (pore size < 2 nm) and mesopores (pore size: 2 – 50 nm). The micropore volume was determined via t-plot method and micropore size distribution by the Dubinin-Asthakov (DA) model. The mesopore volume and pore size distribution were determined using the Barrett-Joyner-Halenda (BJH) model on the desorption branch of the isotherm. The meso- and macropore (pore size > 50 nm) size distribution (0.0036 - 300 µm) of SiO_2 spheres sorbents were determined using a QUANTACHROME PoreMaster mercury intrusion porosimeter with a low-pressure and high-pressure station.

The compressive strength of SiO_2 spheres was measured on a Zwicki Z0.5 with a 20 N and 500 N pressure cell. The measurement was performed for 50 SiO_2

spheres of each sorbent. Prior to the measurement, the particle size of each SiO_2 spheres was determined.

2.3 High pressure thermogravimetric analysis (TGA)

N_2 and CO_2 isotherms were obtained at 35 °C and 70 °C in a range of 0.5 – 40 bar using a Rubotherm magnetic suspension balance (see Figure S 2). Approximately 100 mg (± 0.1 mg) of the sorbent was placed in a steel crucible and dried at 100 °C for 8 h under vacuum prior to adsorption. In order to correct for the buoyancy of the sample in N_2 and CO_2 at different temperatures and pressures, blank adsorption isotherms of non-adsorbing glass spheres (particle size 425 - 600 µm) were determined and subtracted from the isotherms.

2.4 Infrared (IR) spectroscopy

IR spectra of SiO_2 spheres were measured on a Bruker VERTEX 70 spectrometer with a mercury cadmium telluride (MCT) detector. A self-supporting wafer (~ 10 mg·cm^{-2}) was placed in a vacuum IR cell with CaF_2 windows. Prior to measurements, the wafer was activated at 373 K for 1 h under vacuum ($p = 10^{-6}$ mbar). CO_2 was adsorbed on the sample at a partial pressure of 10 mbar and 40 °C. Spectra were taken every 120 seconds. The IR spectra were obtained by collecting 128 scans with a resolution of 4 cm^{-1}, baseline corrected and normalized to the intensity of Si-O overtone resonances in the range of 2095 - 1755 cm^{-1}.

3. Results and discussion

3.1 Impact of the solvent on structural properties and CO_2 physisorption

The influence of the pH on the hydrolysis and condensation in sol-gel processes has been widely discussed over the last decades.[27-31] The pK_a values of the solvents used decrease in the order of aniline (30.6), 2-butanol (17.0) and benzyl alcohol (15.4), inducing a strong dependence of the hydrolysis and condensation rates.[32, 33] Under acidic conditions, the sol-gel process is dominated by a fast rate of hydrolysis, resulting in a high degree of branching,[28] while condensation is most prominent for a pH above 7 leading to a linear structure of the gel.[28] The pH of the precursor solution was in the basic region for all three solvents (aniline: 11.36, butanol: 11.00, benzyl alcohol: 10.64), because it was mainly controlled by the presence of the primary and secondary amine AAMS. A decrease in pH in this range slows down primarily the rate of hydrolysis rather than the condensation rate (Scheme 3).[28] Assuming stationary conditions for the concentration of the hydrated TEOS, a lower pH increases the concentration of the non-hydrated form of TEOS (Scheme 3). Therefore, the overall rate of the formation of the solid gel was retarded, which favors the formation of a linear chain structure in the final polymerized material.

The micro-, meso- and macropore volumes of the SiO_2 spheres using aniline, benzyl alcohol and butanol as a solvent are illustrated in Figure 2. For further assignment, SiO_2 spheres are denoted as aniline, benzyl alcohol and butanol spheres dependent on the solvent employed during synthesis. Whenever a specification is required, SiO_2 spheres without incorporated Zr^{4+} are denoted as aniline, benzyl alcohol and butanol Zr(0). The micropore volume of all SiO_2 spheres was lower than the mesopore volume (Figure 2 a, b). A significant contribution of macropores was only observed for butanol Zr(0) (Figure 2 c). The mesopore volume was lower for butanol Zr(0) compared to aniline and benzyl alcohol Zr(0), due to pronounced hydrolysis leading to a more branched and less-defined mesopore distribution. The most significant impact on the rate of hydrolysis was, however, achieved via the solubility of the solvent in water, surrounding the micelle. It should be noted that two H_2O molecules are needed for the hydrolysis, which will later be regained in the condensation. The solubility of the solvents in water decreased in the order butanol (125 $g \cdot L^{-1}$), benzyl alcohol (40 $g \cdot L^{-1}$) and aniline (36 $g \cdot L^{-1}$).[33] Thus, the

solvents aniline and benzyl alcohol allow only a modest exchange of water and solvent via the surfactants on the outer side of the micelle and lead to very controlled hydrolysis. In contrast, 2-butanol allows a rapid exchange of water molecules via the interface due to its high solubility in water, resulting in an accelerated hydrolysis.[21] Additionally, the strong diffusion gradient results in the formation of large channels, mainly in the interface layer that form macropores after calcination (Figure 2 c).

The BET surface areas and the pore size distributions of the adsorbents are displayed as a function of the solvent and their Zr^{4+} content in Figures 3 and 4, respectively. The large contribution of macropores of butanol spheres leads to a high BET surface area (660 $m^2 \cdot g^{-1}$). SiO_2 spheres synthesized with aniline and benzyl alcohol show similar specific surface areas and mesopore volumes, because the solubility of these solvents in water is approximately identical. The micropore volume of the SiO_2 spheres correlates with the basicity of the solvent and was most pronounced for the solvent with the highest pK_a (Figure 2 a). The mesopore size distribution has a maximum at a larger diameter for benzyl alcohol Zr(0) (31 nm) compared to aniline Zr(0) (15 nm), due to the slightly enhanced condensation rate because of the higher basicity of aniline (Figure 4 a).

The CO_2 and N_2 sorption isotherms of the various SiO_2 spheres are compiled in Figure 5 and the according maximum uptakes are reported in Table 1. Similar CO_2 adsorption characteristics were observed for aniline Zr(0) and benzyl alcohol Zr(0) (Figure 5 a, d). The slightly higher CO_2 uptake at 40 bar and 35 °C of benzyl alcohol Zr(0) is concluded to be a consequence of the higher surface area and micropore volume in comparison to aniline Zr(0) (Table 1, Figure 2 a, b). Nevertheless, the CO_2 uptake at 70 °C of both sorbents showed only a negligible difference (Table 1). The most significant difference in the CO_2 uptake was observed for butanol Zr(0), exhibiting an increased CO_2 uptake capacity already at partial pressures below 20 bar, almost doubling the heat of adsorption compared to aniline Zr(0) (Figure 5, see Table S 7 for ΔH^0_{ads}). The enhanced CO_2 capacity of butanol Zr(0) is attributed to the highest surface area of all SiO_2 spheres resulting from the defined macroporous structure (Figure 2 a, c). Please note that the mean free path length of CO_2 at 20 bar pressures is on the order of ~ 2 nm, which implies that the transport of CO_2 is in the regime of bulk diffusion and therefore pore diffusion limitations can be excluded inside the macropores that are 154 nm in diameter (Figure 4 b).

3.2 Enhanced CO_2 chemisorption and structural effects by incorporation of Zr^{4+}

Zr^{4+} cations were incorporated in the SiO_2 spheres with approximately 1 wt.% (5 wt.% zirconium(IV) *t*-butoxide) and 7 wt.% (25 wt.% zirconium(IV) *t*-butoxide) (Table 2). In accordance to the pure adsorbents, the Zr^{4+} containing SiO_2 spheres are subsequently denoted as aniline, benzyl alcohol, butanol Zr(1) and Zr(7). Addition of 25 wt.% zirconium(IV) *t*-butoxide (based on TEOS) to the precursor solution resulted in an instant drop of pH by approximately 0.2 for all precursor solutions independently of the solvent used. The full hydrolysis of zirconium(IV) *t*-butoxide, and the subsequent formation of more than four-coordinated Zr^{4+} complexes in an alkaline environment, results in the net consumption of hydroxyl groups and therefore a decrease in pH. Because the overall content of zirconium(IV) *t*-butoxide is rather low compared to the other silanes, cross-condensation is most likely favored over self-condensation. Moreover, in contrast to acid catalyzed hydrolysis, the hydrolysis rate increased with every additional hydrolysis per molecule.[31, 34] Thus, zirconium(IV) *t*-butoxide leads to an accelerated hydrolysis of all alkoxides and, therefore, to a higher degree of crosslinking inside the SiO_2 particles due to the formation of pre-condensed units leading to significant decline in the accessibility of the pores of the SiO_2 spheres, independently of the solvent used.[28]

The marked decrease of the macropore volume from 1.207 to 0.233 $cm^3 \cdot g^{-1}$ upon incorporation of 7 wt.% Zr^{4+} in SiO_2 spheres synthesized with butanol is shown in Figure 4. No defined macroporous structure was observed for benzyl alcohol SiO_2 spheres (Figure 4 b, d, f). The macropore volume of aniline spheres increased with an increasing Zr^{4+} content, but still remained moderate without a defined distribution (Figure 4 b, d, f). Aniline and benzyl alcohol SiO_2 spheres underwent a significant decrease in mesopore volume from 0.544 to 0.374 $mL \cdot g^{-1}$ and 0.533 to 0.170 $mL \cdot g^{-1}$ with 7 wt.% Zr^{4+}. (Figure 2 b). Significant changes were not observed when Zr^{4+} was inserted in butanol SiO_2 spheres, because only a small percentage of macropores was transformed into mesopores for higher Zr^{4+} contents (Figure 2 b). Increasing the Zr^{4+} content of aniline spheres also resulted in a decrease of the mesopore size, whereas butanol Zr(1) and Zr(7) mainly retained an undefined structure (Figure 4 a, c, e). The mesopore size distribution of benzyl alcohol Zr(1) and Zr(7) spheres narrowed down drastically to approximately 4 Å (Figure 4 c, e). Incorporation

of Zr^{4+} in aniline and benzyl alcohol SiO_2 spheres only resulted in a minor decline of BET surface areas, whereas the decrease was more obvious for butanol Zr(1) and Zr(7) (660 – 554 $m^2 \cdot g^{-1}$) due to a strong collapse of the macroporous structure (Figure 3, Figure 4 f).

The X-ray diffractograms of all SiO_2 spheres showed only one broad peak at $2\Theta = 25°$ and sharp reflections were not observed (see Figure S 5). The diffractograms remained unchanged after incorporation of Zr^{4+} in the framework, which indicates that crystalline ZrO_2 domains with long-range order were absent.[34] Therefore, we conclude that Zr^{4+} cations were dispersed in the silica structure. The SEM images of aniline, benzyl alcohol and butanol spheres with 0, 1 and 7 wt.% Zr^{4+} are shown in Figure 6. An undefined increase in pore size was observed by SEM for aniline spheres, when zirconium(IV) *t*-butoxide was added to the precursor solution. The loss of a defined pore structure for benzyl alcohol and butanol spheres upon incorporation of 7 wt.% Zr^{4+} was observed. An ordered macroporous structure was solely observed for butanol spheres at Zr^{4+} concentrations up to 1 wt.% (Figure 6) that was in accordance with the results of the macropore volume distribution (Figure 2, Figure 4).

The heat of CO_2 adsorption (ΔH^0_{ads}) was below 18 $kJ \cdot mol^{-1}$ for all SiO_2 spheres (see Table S 7). The determination of the heat of adsorption (ΔH^0_{ads}) for CO_2 from a Langmuir type isotherm did not correlate to the Zr^{4+} content of the sorbents. Structural changes of SiO_2 spheres prepared with different solvents influence the accessibility of Zr^{4+} cations and therefore ΔH^0_{ads}. Incorporation of Zr^{4+} resulted only in a marginal increase of CO_2 storage capacity for aniline spheres, whereas the uptake increased by 15 % for benzyl alcohol spheres when 1 wt.% Zr^{4+} was incorporated and decreased significantly for 7 wt.% Zr^{4+} (Figure 5, Table 1). The highest CO_2 uptakes were observed for butanol Zr(0) (25.8 wt.%) and butanol Zr(1) (26.2 wt.%) at 35 °C and a pressure of 40 bar CO_2. Further incorporation of Zr^{4+} also resulted in a decrease of the maximum CO_2 storage capacity. Noteworthy, the uptake capacity for CO_2 still remained at reasonable capacity for all adsorbents. The CO_2 uptake is linearly correlated to the BET surface area of all SiO_2 spheres independent of the Zr^{4+} content (Figure 7a). Zeolite 13X showed an enhanced uptake due to strong interaction of CO_2 with the Na^+ cations (Figure 7 a, Figure 7 b), while SBA-15 followed the trend of the SiO_2 spheres. However, the CO_2 uptake capacity did not

depend on the pore volume for all samples investigated (see Table S 3 and Table S 5). The general increase in adsorption capacity for low Zr^{4+} contents (1 wt.%) resulted in a moderate decrease in the free pore volume and surface area, but enhanced CO_2 physisorption due to the stronger interaction of CO_2 with the oxygen Lewis base sites neighboring Zr^{4+} (Figure 3, Figure 7 b). With increasing Zr^{4+} concentration, the decrease in the pore volume was more pronounced which led in turn to a decrease of the accessibility of Zr^{4+} sites and to a decrease of CO_2 adsorption capacity (Figure 3, Figure 7 b).

The differences in the IR spectra after adsorption of 10 mbar CO_2 on SiO_2 spheres with 0 and 7 wt.% Zr^{4+} as revealed by the IR spectra of adsorbed CO_2 are illustrated in Figure 8. The spectra shown in Figure 8 were obtained by subtracting the spectra of the samples in contact with CO_2 from the spectra of the samples before adsorption. Therefore, in this figure bands increasing in intensity point upwards, while bands decreasing in intensity point downwards. Regions in the IR spectra not affected by the interaction with CO_2 remain unchanged. Please note, that the CO_2 adsorption was performed only at 10 mbar, because at higher pressures sensitivity is lost due to an overlap with gas phase CO_2. The samples have been dried for 1 h at 373 K under vacuum prior to adsorption in order to exclude influences of adsorbed H_2O on the adsorption of CO_2. The difference between the IR spectra of activated aniline, benzyl alcohol and butanol Zr(0) and SiO_2 in presence of 10 mbar CO_2 showed a band at 1633 cm^{-1} (Figure 8), which is assigned to the asymmetric stretching vibration of a bridged bidentate bicarbonate species (Scheme 4, III).[35, 36] The corresponding symmetric stretching vibration is expected at a 400 cm^{-1} lower frequency and could, therefore, not be recorded due to the strong IR absorption of the SiO_2 matrix in this region.[35, 37] Independently of the solvent used, the CO_2 adsorption was more pronounced for Zr^{4+} containing SiO_2 spheres. Incorporation of Zr^{4+} resulted in three additional bands in the range of 1505 – 1380 cm^{-1} that were most pronounced for benzyl alcohol Zr(7) (Figure 8, see Table S 6 for integrated areas) and the bands around 1500 cm^{-1} and 1460 cm^{-1} showed a significant overlap independent of the employed solvents. The band of b-HCO_3^- at 1633 cm^{-1} was strongly overlapped by an intense new peak at 1610 cm^{-1} that was assigned to the asymmetric stretching vibration of bidentate bicarbonates on Zr^{4+} (b-HCO_3^--Zr) (Scheme 4, II).[36-38] The corresponding symmetric stretching vibration of b-HCO_3^--Zr

was observed at 1460 cm^{-1}.[36, 37, 39] In contrast to SiO_2 spheres without Zr^{4+}, b-HCO_3^- species can additionally be formed on one surface metal atom, resulting in a stronger bound surface species (Scheme 4). The bands at 1500 cm^{-1} (asymmetric) and 1380 cm^{-1} (symmetric) are assigned to monodentate carbonate species (m-CO_3^{2-}-Zr) as illustrated in Scheme 4 I.[35, 37] In summary, only one Zr^{4+} surface site is needed for the adsorption of CO_2, whereas two Si atoms are required for the stabilization of a surface bound bicarbonate species.

3.3 Applicability of SiO_2 spheres for pressure swing (PSA) and temperature swing adsorption (TSA)

SBA-15 and zeolite 13X were selected as benchmark materials to evaluate the potential of Zr^{4+} containing SiO_2 spheres for CO_2 pre-combustion adsorption processes. The uptake of CO_2 and N_2 over the benchmark materials is compared to the uptake of Zr^{4+} containing SiO_2 spheres in Figure 9. CO_2 adsorbed mainly via bidentate bicarbonate species (b-HCO_3^-) inside the pores of mesoporous SBA-15, whereas the microporous zeolite 13X interacts with CO_2 preferably via the oxygen Lewis base sites neighboring Na^+ cations.[40] It should be further noted, that SBA-15 has not only a higher surface area compared to microporous zeolite 13X (737 and 608 $m^2 \cdot g^{-1}$, respectively), but also the total pore volume is roughly 3 times higher (Table 3). Both benchmark sorbents have a well-defined pore size distribution (see Figure S 4). The shape of the adsorption isotherms of SBA-15 exhibited a strongly preferred adsorption of CO_2 compared to N_2 over the entire pressure range up to 40 bar at 35 °C and 70 °C (Figure 9). The slope of CO_2 adsorption isotherms of zeolite 13X was steeper at partial pressures below 10 bar compared to SBA-15 and remained almost constant for higher pressures. The heat of adsorption, determined from the sorption isotherms, for CO_2 was over three times higher for zeolite 13X (30 $kJ \cdot mol^{-1}$) than SBA-15 (9 $kJ \cdot mol^{-1}$). At 35 °C the sorption capacity for CO_2 was almost the same for SBA-15 (32.4 wt.%) and zeolite 13X (32.5 wt.%), whereas at 70 °C the CO_2 uptake of 13X is more than 10 % higher compared to SBA-15 (Table 1). Independent of the adsorption temperature, SBA-15 adsorbed less N_2 than zeolite 13X (Figure 10 and Table 1). The sorption isotherms of SiO_2 spheres indicate a high selectivity for CO_2 over N_2 and had a shape similar to the isotherms of SBA-15 (Figure 5, Figure 9). The performance of all sorbents was evaluated for pressure

swing (PSA; 40 to 1 bar at 35 °C) and temperature swing (TSA; 35 °C to 75 °C at 40 bar) adsorption by calculating the difference in uptake from the CO_2 and N_2 sorption isotherms (Figure 5, Figure 9). As mentioned earlier, it was not possible to determine H_2 adsorption in our set-up up to 40 bar. However, it was possible to determine the adsorption of H_2 on one selected adsorbent (butanol SiO_2 spheres) up to a maximum pressure of 30 bar (Figure S 6). The adsorption of H_2 was comparably low as the adsorption of N_2 and therefore the quantitative assumption of PSA and TSA operating methods are applicable in pre-combustion applications (Figure 5, Figure S 6). Because the heat of adsorption of CO_2 and hence the steepness of the isotherm was so much more pronounced than that of N_2, competitive gas adsorption of CO_2 and N_2/H_2 was not performed.

The flue gas composition of a typical pre-combustion process of roughly 40 % CO_2 and 60 % H_2 results in a CO_2 to H_2 ratio of 2/3.[41] SBA-15 exhibits the best adsorption ratio of CO_2 over N_2 with 14.4 (TSA) and 8.6 (PA). 13X zeolite on the other hand is not applicable under these high pressure separation conditions, since the steep isotherm results in a CO_2 over N_2 ratio of only 2.7 (TSA) and 1.3 (PSA).[42] The maximum CO_2 uptake of SiO_2 spheres increased for 1 wt.% Zr^{4+} and decreased for the materials with higher Zr^{4+} concentrations independently of the solvents used (Figure 10). The studied SiO_2 spheres had ratios of the adsorbed concentrations of CO_2 and N_2 of 3.6 (butanol Zr(0) and Zr(1)) to 6.4 (benzyl alcohol Zr(0)) for temperature swing separation and between 5.8 (aniline Zr(7)) and 6.6 (butanol Zr(7)) for pressure swing separation. The separation ratios were significantly higher on all SiO_2 spheres than on zeolite 13X, both in TSA and PSA applications, thus these adsorbents are a promising alternative to SBA-15 in PSA processes. While small concentrations of Zr^{4+} in the SiO_2 spheres appear to be beneficial, it is difficult to derive a generalized influence of the Zr^{4+} content on the separation performance of CO_2 over N_2, because in addition to the chemical modifications also structural changes (varying with the solvent) were induced upon incorporation of Zr^{4+}.

The long-term stability of the sorbent is a key feature of a cost-effective separation process. Hence, the compressive strength of SiO_2 spheres is compiled for the solvents and Zr^{4+} contents applied (Figure 11, Table 4). Additionally, the compressive strength was plotted over the according particle size of 50 SiO_2 spheres for each sorbent (Figure 12). The particle size distribution was symmetric for aniline

and benzyl alcohol spheres with a maximum around 1.3 mm (Figure 12, Table 4). Butanol spheres had a less defined particle size distribution, which is attributed to the strong solvent exchange across the micelle interface (Figure 12). The average particle size, however, was also approximately 1.3 mm (Table 4).

The average compressive strength of the SiO_2 spheres increased upon incorporation of Zr^{4+} independent of the used solvents (Table 4). Aniline spheres exhibited the highest mechanical stability of all sorbents because of the accelerated condensation induced by the solvent with the highest pK_a (Figure 11, Table 4). The lowest compressive strength was observed for butanol spheres, because both butanol Zr(0) and Zr(1) have a compressive strength lower than 20 N (Figure 11). The significant increase in stability of butanol Zr(7) was in accordance with the total loss of the macroporous structure. Overall, the incorporation of Zr^{4+} led to a larger differences between the compressive strengths. We speculate that the concentration of Zr^{4+} cations is too low to compensate for the lack of long range order, leading to reduced stability of the spheres. Thus, it can be concluded that a defined stability of the SiO_2 spheres is limited by the content of Zr^{4+} that can be incorporated in the SiO_2 framework.

5. Conclusions

Hierarchically structured spherical sorbent for the separation of CO_2 and N_2 for pre-combustion applications have been explored. The significant influence of the solvents on the morphology of the SiO_2 spheres did not only correspond to the solvents basicity, but also on the solubility in H_2O, which both strongly influenced the interactions via the borders of the micelles resulting in the formation of a macroporous structure. The use of aniline and benzyl alcohol as a solvent for the synthesis resulted in micro- and mesopores in the spherical sorbents, whereas butanol led to an additional and well-defined macroporous structure. SiO_2 spheres prepared with butanol combined a macropore volume of 1.2 $mL \cdot g^{-1}$ with micropore and mesopore volumes of 0.1 $mL \cdot g^{-1}$ and 0.38 $mL \cdot g^{-1}$, respectively. Zr^{4+} was successfully incorporated in the framework structure of the SiO_2 spheres. The presence of Zr^{4+} enhanced the CO_2 interaction, but the uptake capacity was limited because a lower micro- and mesopore volume reduced the sorption capacity. The accelerated hydrolysis caused by the Zr alkoxides resulted in a less ordered and more branched structure of the framework. Even as the pore volumes decreased with higher concentrations of Zr^{4+} cations, the still relatively large pore volumes make the spheres a highly interesting alternative to zeolite 13X and SBA-15 in pressure swing and temperature swing pre-combustion processes. The stability of the sorbents increases for higher Zr^{4+} contents improving the long-term stability of the SiO_2 spheres.

Acknowledgments

We would like to thank the federal Ministry of Education and Research (BMBF) for financial support (project no. 01RC1106A). Financial support from the DFG under the project LE 1187/10 is gratefully acknowledged. Additionally, we would like to thank Clariant, Siemens and Zeta Partikelanalytik for productive discussions in the iC^4 AdCOO project. We thank WACKER and BASF for providing chemicals. We thank Franz Xaver Hecht and Martin Neukamm for technical support. Additionally, we would like to thank Prof. Dr.-Ing. Kai-Olaf Hinrichsen and Ursula Herrmann for N_2 physisorption measurements in the framework of Municat. We also would like to thank Prof. Dr. Johann Plank, Johanna de Reese and Timon Echt for Hg porosimetry measurements. Furthermore, we also would like to thank Andreas Berger and Korina Hartmann for scientific contribution during their Master's studies.

Supporting information

Flow sheets of set-ups as well as detailed information on the reactor column, SBA-15 synthesis, elemental analysis and Langmuir calculations are provided. Additional graphs of N_2 physisorption isotherms and BET surface areas, pore volumes as well as pore size distributions are available. Furthermore, X-ray diffractograms and data of adsorption isotherms are also provided.

Appendices

Schemes

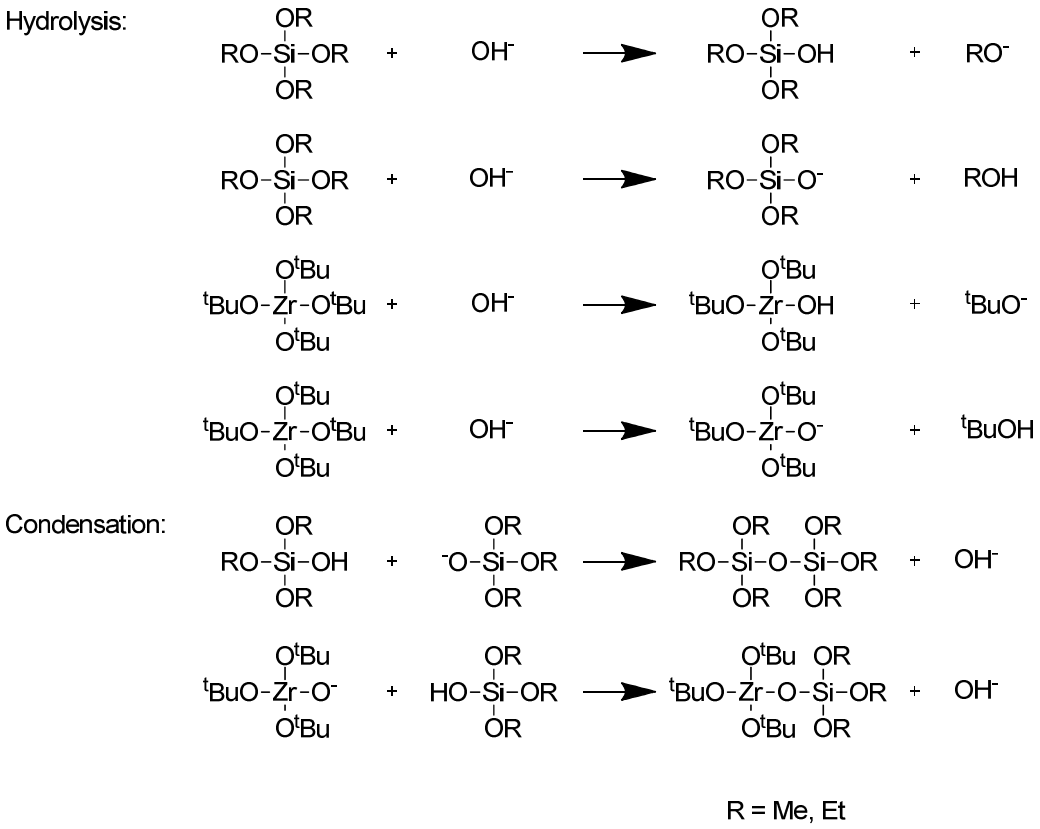

Scheme 1 Hydrolysis and condensation reactions during synthesis of SiO_2 spheres.

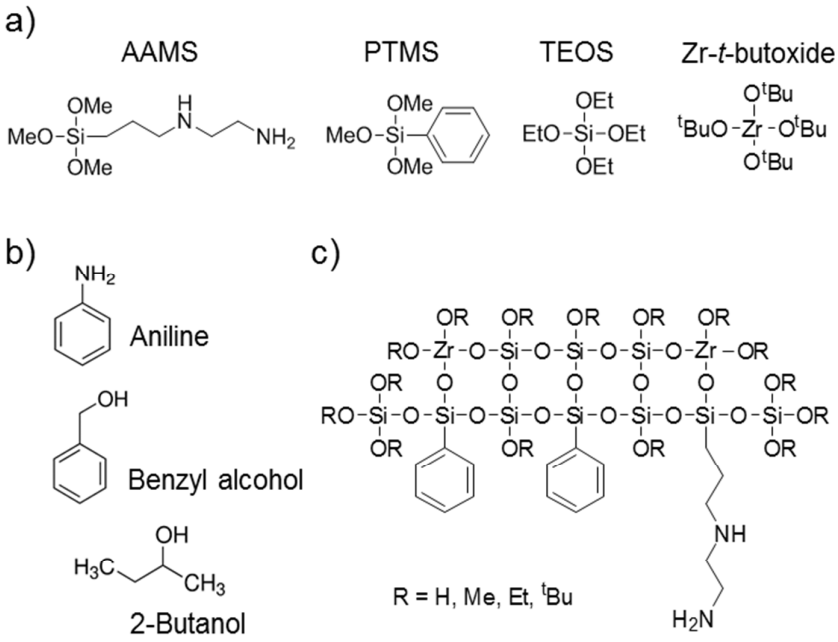

Scheme 2 (a) Structure directing compounds, (b) solvents and (c) proposed coordinative structure prior to calcination.

Rate of hydrolysis $$r_{hydrolysis} = k_{hydrolysis} \cdot [TEOS] \cdot [OH^-]$$

Rate of condensation $$r_{condensation} = k_{condensation} [TEOS_{hydrated}]^2$$

Stationary conditions $$\frac{d[TEOS_{hydrated}]}{dt} = r_{hydrolysis} - r_{condensation} \approx 0$$

$$[OH^-] = \frac{k_{condensation}}{k_{hydrolysis}} \cdot \frac{[TEOS_{hydrated}]^2}{[TEOS]}$$

$$[H^+] = \frac{K_w \cdot k_{hydrolysis}}{k_{condensation}} \cdot \frac{[TEOS]}{[TEOS_{hydrated}]^2} \quad \text{with} \quad [H^+] \cdot [OH^-] = K_w$$

$$pH = -\log\left\{ \frac{K_w \cdot k_{hydrolysis}}{k_{condensation}} \cdot \frac{[TEOS]}{[TEOS_{hydrated}]^2} \right\}$$

Scheme 3 pH dependency of the hydrolysis of TEOS.

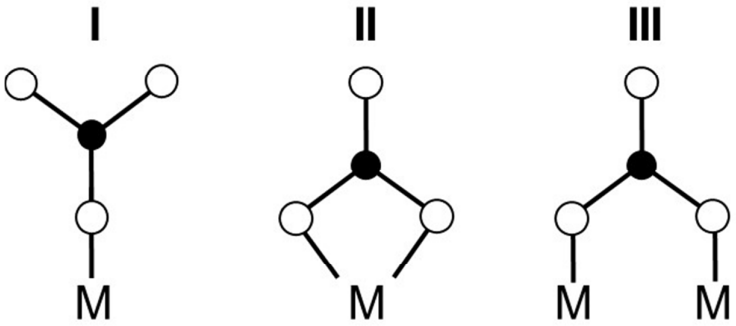

Scheme 4 Simplified illustration of potential carbonate surface species of CO_2 bound on SiO_2 spheres. (I) Monodentate carbonate, (II) bidentate bicarbonate, (III) bridged bidentate bicarbonate. M represents the according metal site.

Figures

Figure 1 Proposed structure of SiO_2 spheres according to Scholz et al.[23, 25]

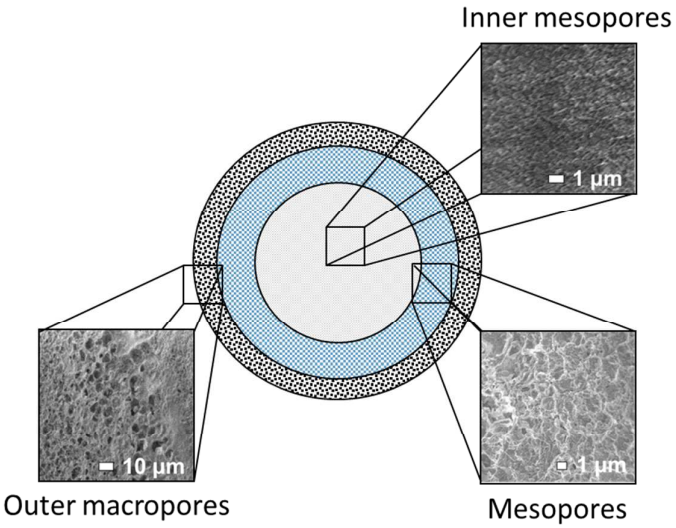

Figure 2 Micro[a] (a), meso[a] (b) and macro[b] (c) pore volume of aniline, benzyl alcohol and butanol Zr(0) (dots), Zr(1) (horizontal lines) and Zr(7) (diagonal lines). [a] Determined by N_2 physisorption, [b] determined by Hg porosimetry.

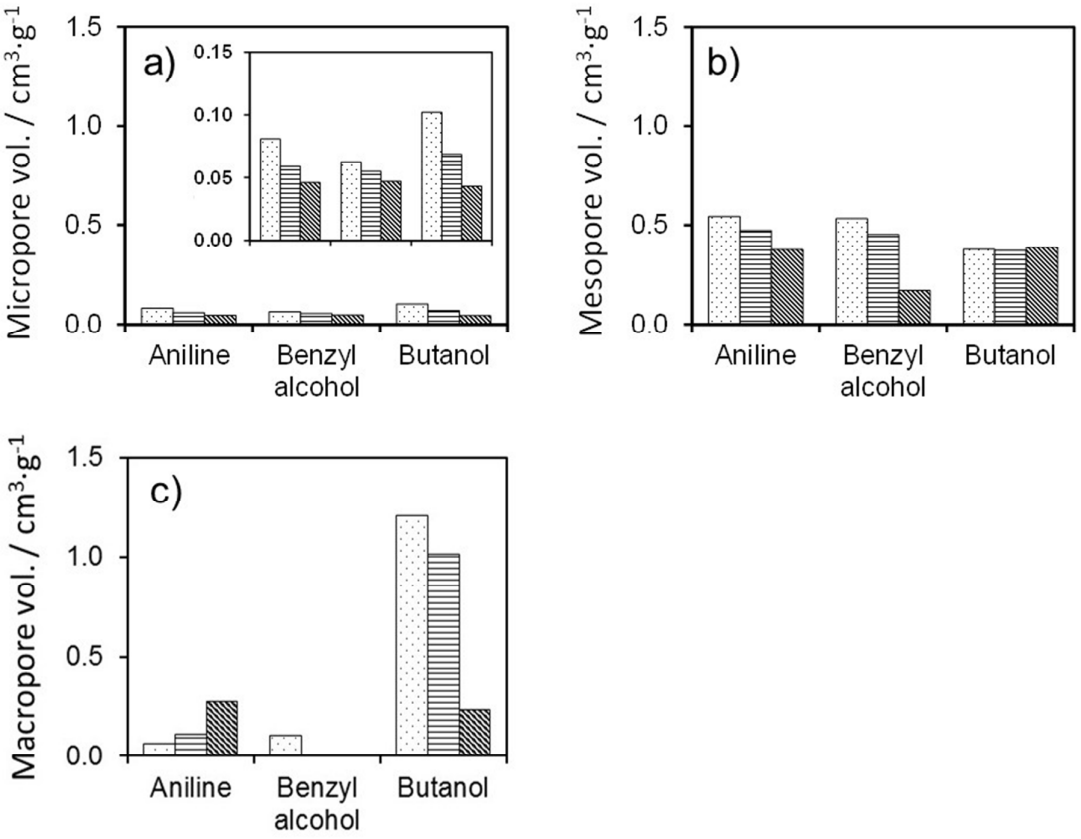

Figure 3 BET surface area of aniline, benzyl alcohol and butanol Zr(0) (dots), Zr(1) (horizontal lines) and Zr(7) (diagonal lines).

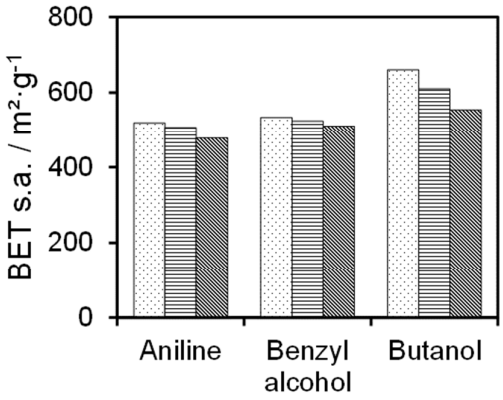

Figure 4 Pore size distribution of aniline (solid line), benzyl alcohol (dashed line) and butanol (dotted line) Zr(0) (a-b), Zr(1) (c-d) and Zr(7) (e-f) determined by N_2 physisorption (a, c, e) and Hg porosimetry (b, d, f). Figure 4c was additionally enlarged in the range of 2 to 8 nm.

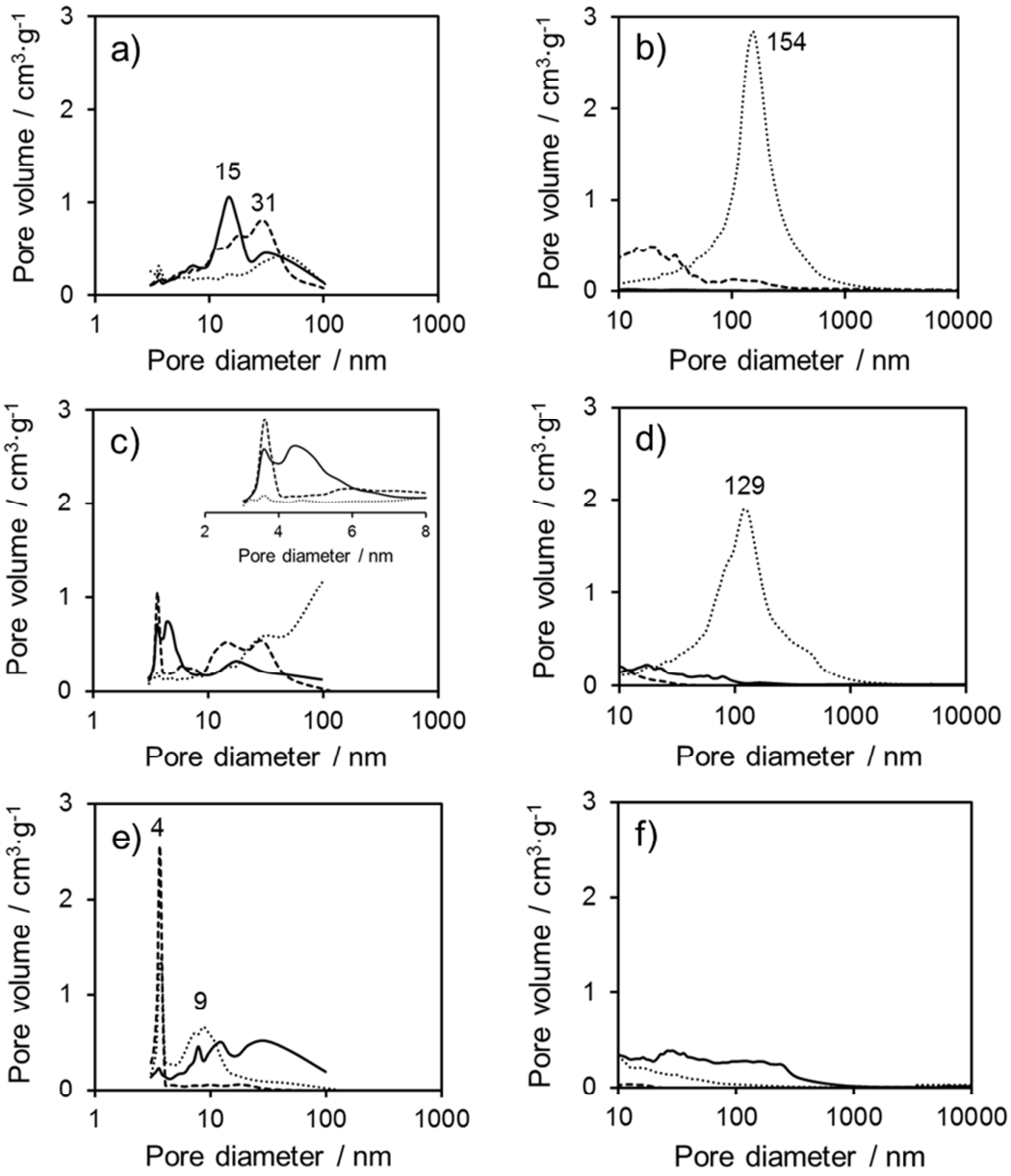

Figure 5 CO_2 adsorption (circles) and N_2 adsorption (squares) at 35 ℃ (filled symbols) and 70 ℃ (unfilled symbols). (a-c) Aniline, (d-f) benzyl alcohol and (g-h) butanol Zr(0) (a, d, g), Zr(1) (b, e, h) and Zr(7) (c, f, i).

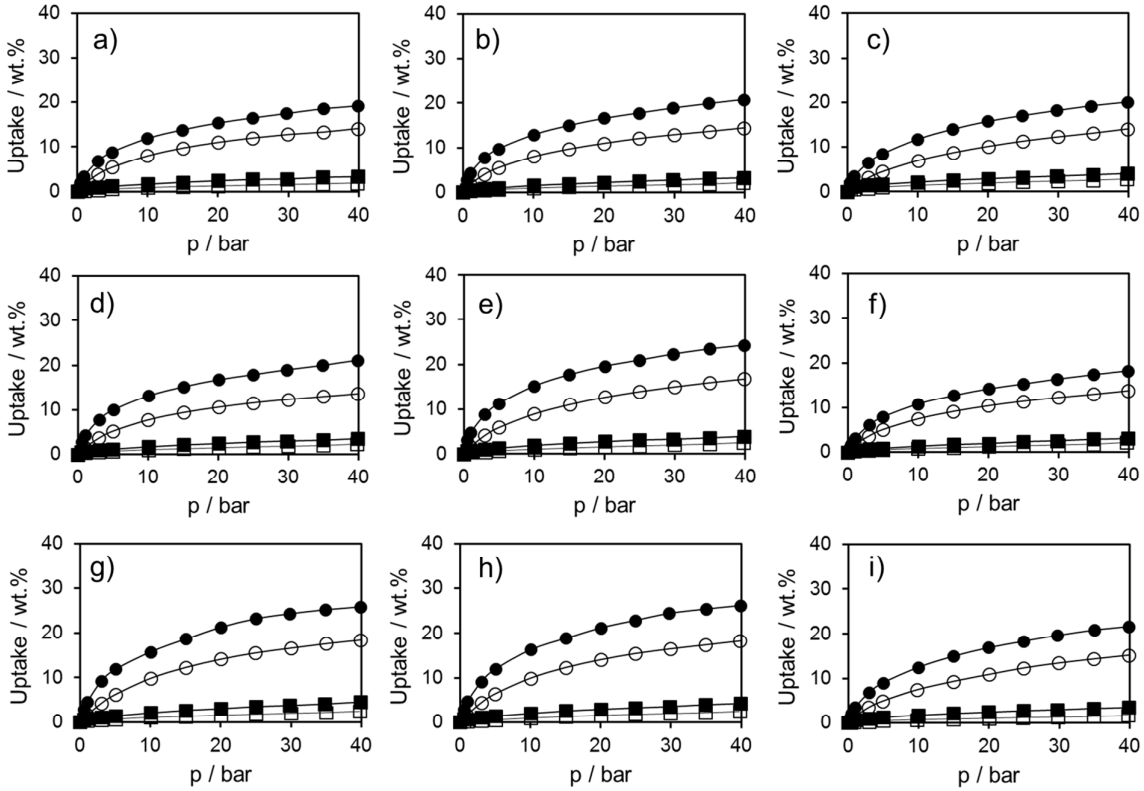

Figure 6 SEM images of (a-c) aniline, (d-f) benzyl alcohol and (g-i) butanol Zr(0) (a, d, g), Zr(1) (b, e, h) and Zr(7) (c, f, i).

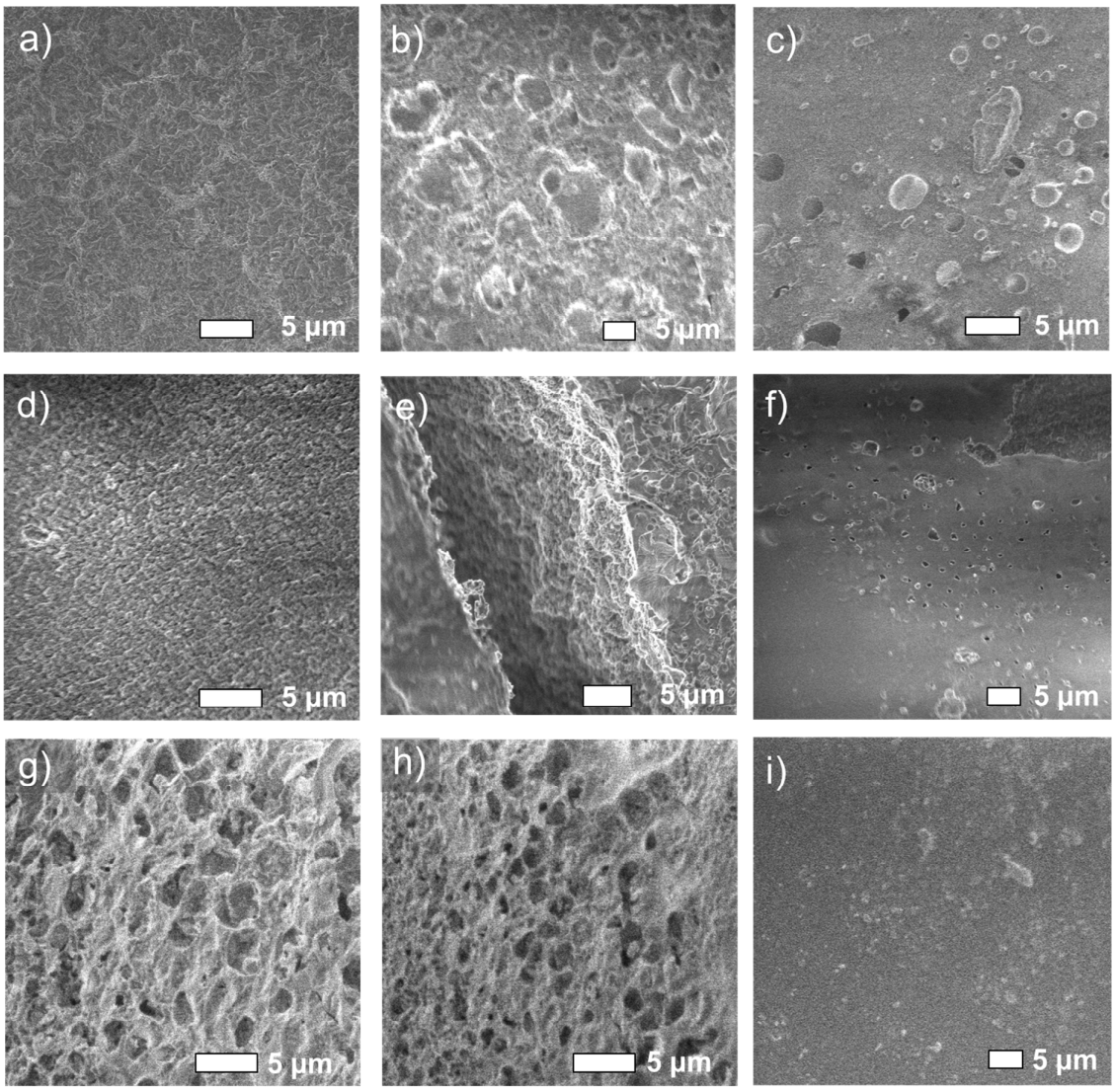

Figure 7 (a) Correlation between the CO_2 uptake (35 °C, 40 bar) and BET surface area and (b) influence of Zr^{4+} content on the normalized uptake capacity. SBA-15 (non-filled circle), zeolite 13X (filled circle) and aniline (triangle), benzyl alcohol (diamond) and butanol (square) spheres with varying Zr^{4+} concentrations.

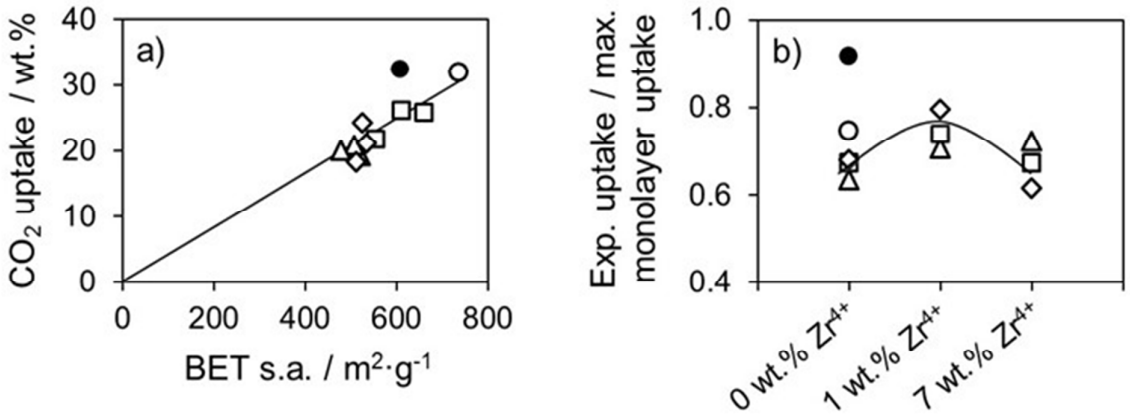

Figure 8 IR difference spectra of (a) aniline, (b) benzyl alcohol and (c) butanol Zr(0) (I) and Zr(7) (II) at 10 mbar CO_2 partial pressures. Spectra were taken every 120 seconds. The intensities of the characteristic IR bands increase with exposure time.

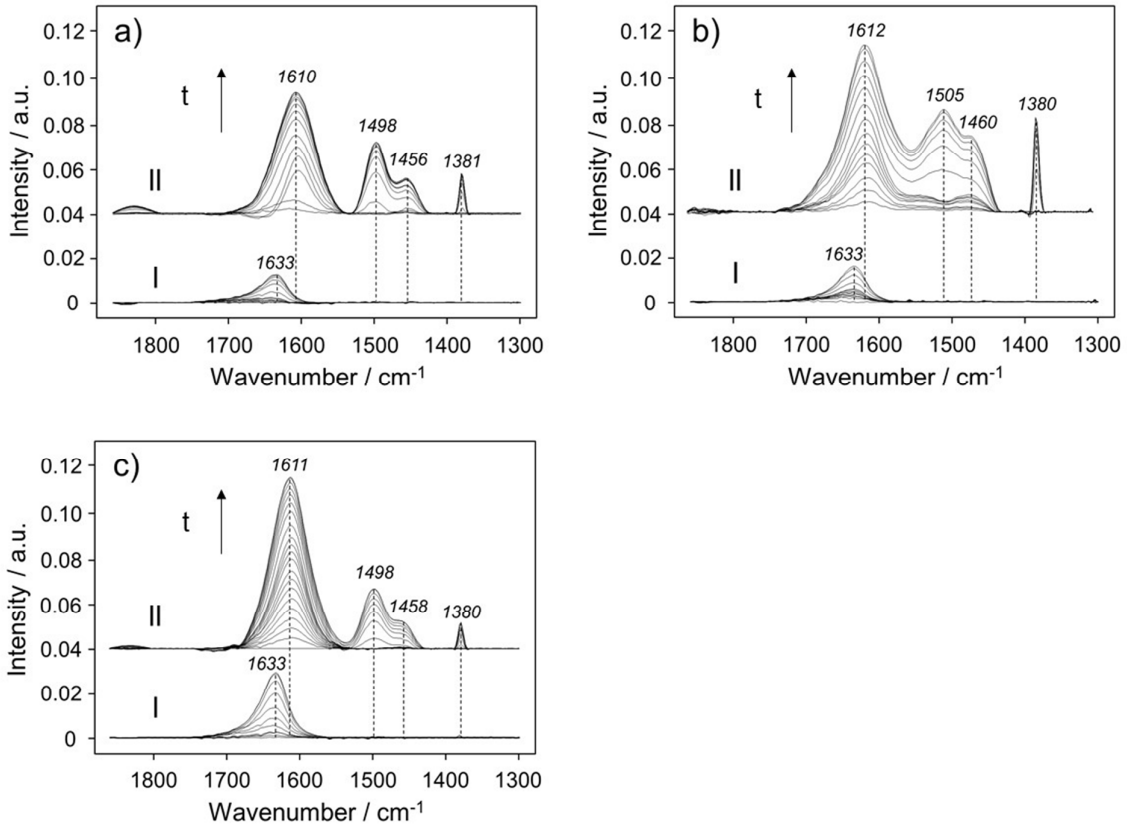

Figure 9 CO_2 adsorption (circles) and N_2 adsorption (squares) at 35 ℃ (filled symbols) and 70 ℃ (unfilled symbols) of (a) SBA-15 and (b) zeolite 13X.

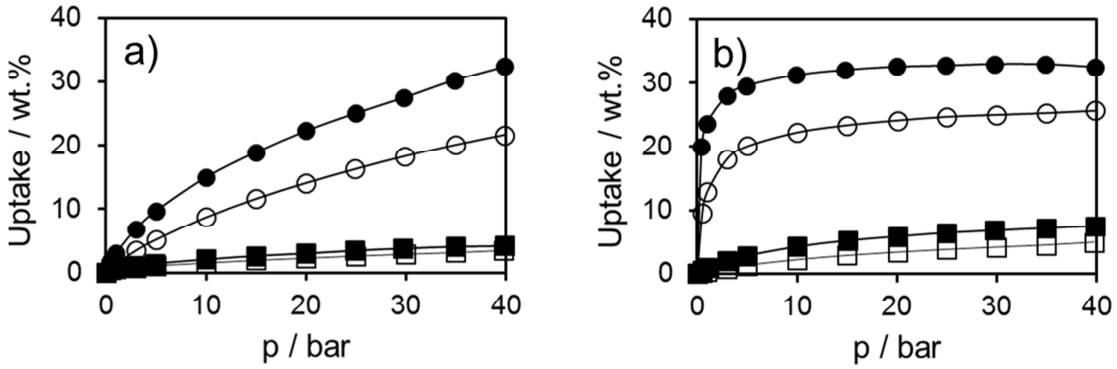

Figure 10 Difference in uptake of the sorbent for the desorption step in temperature swing adsorption (35 ℃ to 70 ℃; (a) CO_2, (b) N_2) and pressure swing adsorption (40 to 1 bar; (c) CO_2 ,(d) N_2). Aniline, benzyl alcohol and butanol Zr(0) (dots), Zr(1) (horizontal lines) and Zr(7) (diagonal lines).

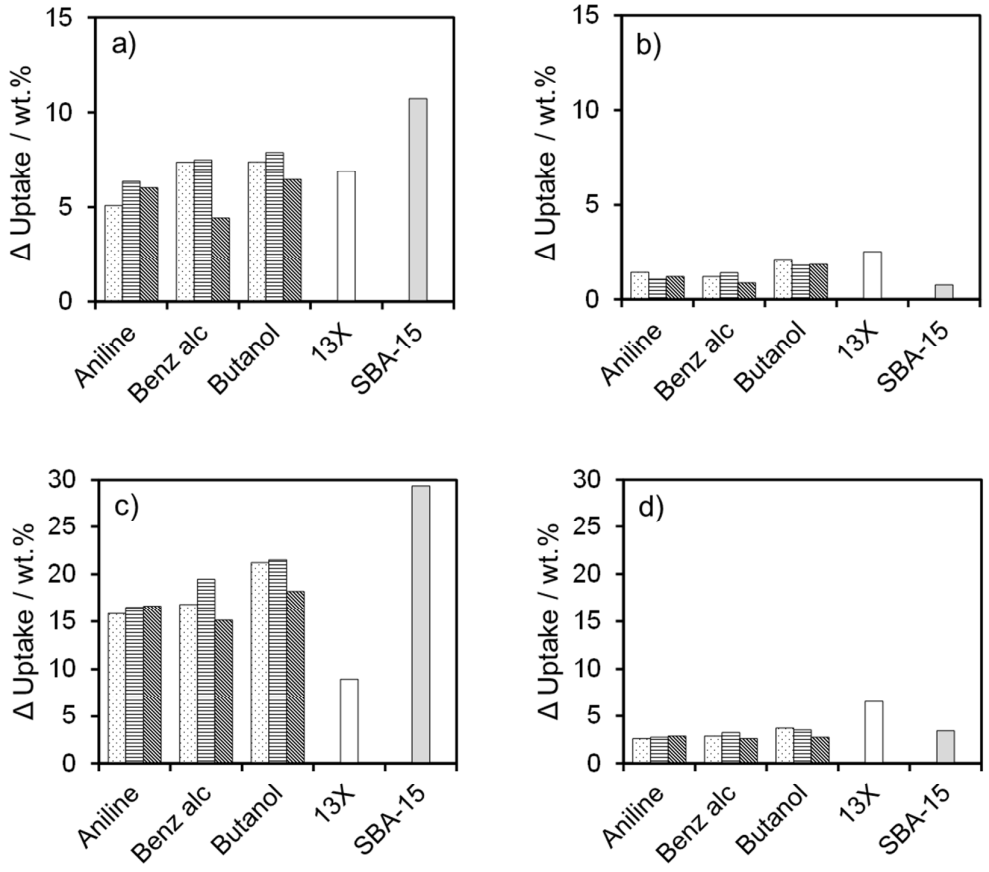

Figure 11 Compressive strength of (a) aniline, (b) benzyl alcohol and (c) butanol Zr(0) (dots), Zr(1) (horizontal lines) and Zr(7) (diagonal lines).

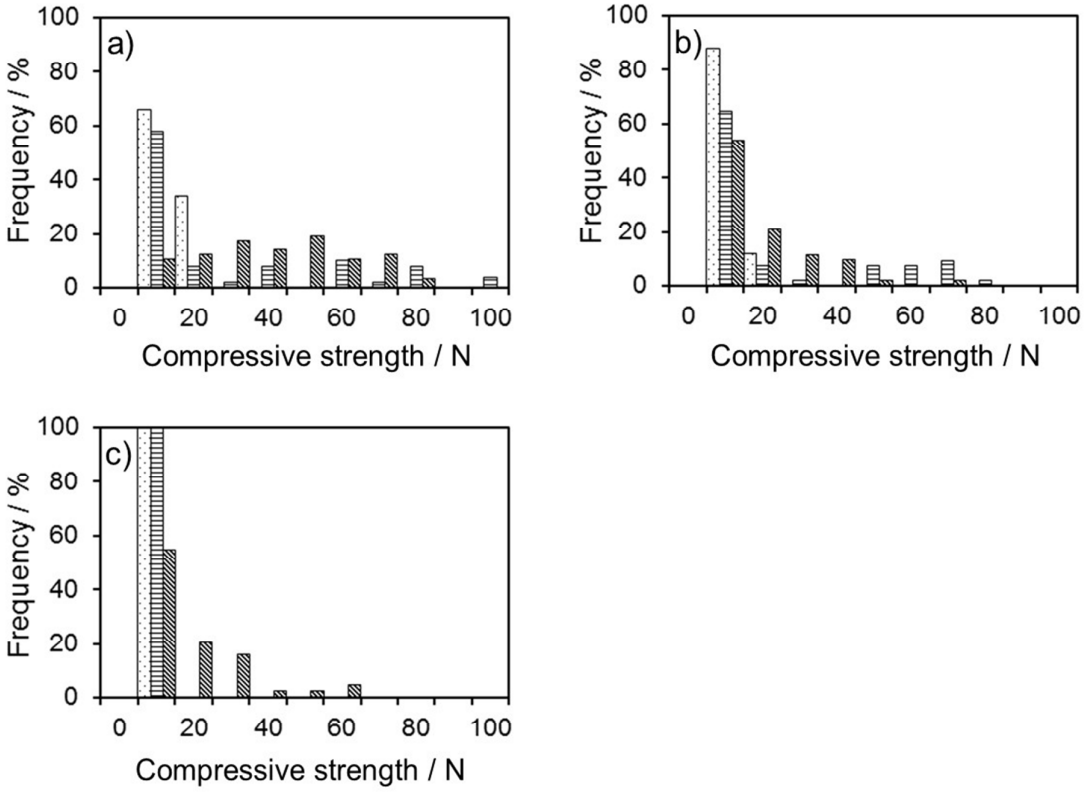

Figure 12 Compressive strength over the particle size of (a-c) aniline, (d-f) benzyl alcohol and (g-i) butanol Zr(0) (a, d, g), Zr(1) (b, e, h) and Zr(7) (c, f, i).

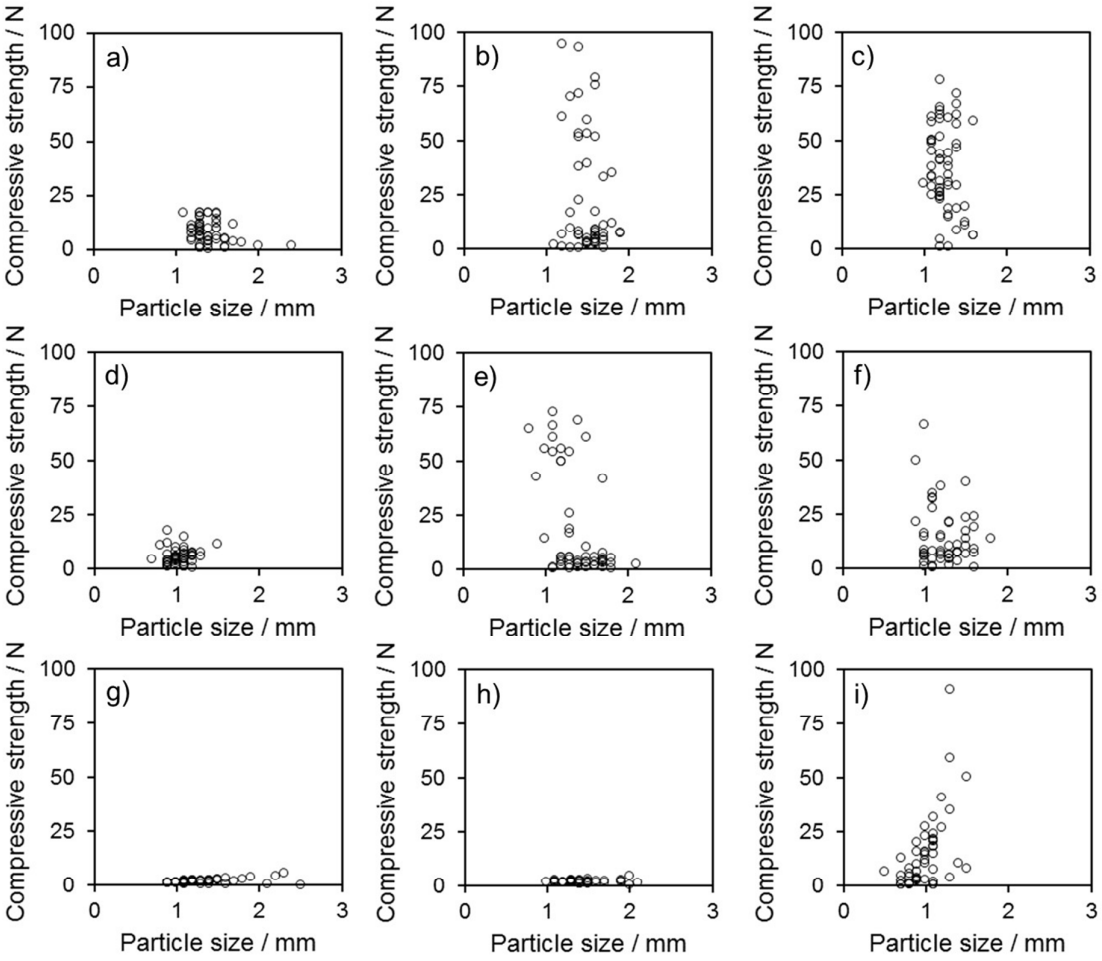

Tables

Table 1 CO_2 and N_2 uptake at 35 °C and 70 °C at a total pressure of 40 bar.

	CO_2 [wt.%]		**N_2** [wt.%]	
	35 °C	70 °C	35 °C	70 °C
SBA-15	32.4	21.7	4.2	3.5
Zeolite 13X	32.5	25.6	7.5	4.9
Aniline Zr(0)	19.2	14.1	3.3	1.9
Aniline Zr(1)	20.8	14.4	3.2	2.2
Aniline Zr(7)	20.1	14.1	4.0	2.8
Benzyl alcohol Zr(0)	21.1	13.7	3.5	2.3
Benzyl alcohol Zr(1)	24.3	16.8	3.9	2.5
Benzyl alcohol Zr(7)	18.3	13.8	3.0	2.2
Butanol Zr(0)	25.8	18.4	4.5	2.4
Butanol Zr(1)	26.2	18.3	4.2	2.5
Butanol Zr(7)	21.7	15.2	3.5	1.6

Table 2 Zr elemental analysis of SiO_2 spheres.

	Zr [wt.%]
Aniline Zr(1)	1.17
Aniline Zr(7)	6.30
Benzyl alcohol Zr(1)	1.15
Benzyl alcohol Zr(7)	7.20
Butanol Zr(1)	1.19
Butanol Zr(7)	7.00

Table 3 BET surface area, pore volume and average pore size of SBA-15 and zeolite 13X. [a] Pore size smaller than 2 nm determined by t-plot method, [b] pore size of 2 to 50 nm determined by BJH method (desorption branch).

Adsorbent	BET surface area [$m^2 \cdot g^{-1}$]	Micropore volume[a] [$cm^3 \cdot g^{-1}$]	Mesopore volume[b] [$cm^3 \cdot g^{-1}$]	Average pore size[b] [nm]
SBA-15	737	0	0.840	6.6 [c]
Zeolite 13X	608	0.277	0.018	0.78 [d]

Table 4 Compressive strength and average diameter of SiO_2 spheres.

	Average compressive strength [N]	**Average spherical diameter** [mm]
Aniline Zr(0)	8.1	1.4
Aniline Zr(1)	23.5	1.5
Aniline Zr(7)	36.7	1.3
Benzyl alcohol Zr(0)	5.4	1.1
Benzyl alcohol Zr(1)	18.5	1.4
Benzyl alcohol Zr(7)	14.2	1.3
Butanol Zr(0)	1.8	1.3
Butanol Zr(1)	1.9	1.4
Butanol Zr(7)	14.8	1.0

Notes and references

1 B. Jiang, Z. Q. Sun and M. Q. Liu, *Energy*, 2010, **35**, 4257-4264.
2 H. Liming, *Renew Sust Energ Rev*, 2009, **13**, 1096-1103.
3 A. J. Ragauskas, C. K. Williams, B. H. Davison, G. Britovsek, J. Cairney, C. A. Eckert, W. J. Frederick, J. P. Hallett, D. J. Leak, C. L. Liotta, J. R. Mielenz, R. Murphy, R. Templer and T. Tschaplinski, *Science*, 2006, **311**, 484-489.
4 F. Manzano-Agugliaro, A. Alcayde, F. G. Montoya, A. Zapata-Sierra and C. Gil, *Renew Sust Energ Rev*, 2013, **18**, 134-143.
5 P. Pongsoi and S. Wongwises, *Renew Sust Energ Rev*, 2013, **24**, 586-592.
6 J. Li, X. G. Zhuang, X. Querol, O. Font, N. Moreno and J. B. Zhou, *Fuel*, 2012, **95**, 446-456.
7 D. J. Hofmann, J. H. Butler and P. P. Tans, *Atmos Environ*, 2009, **43**, 2084-2086.
8 J. Oexmann and A. Kather, *Enrgy Proced*, 2009, **1**, 799-806.
9 M. Kanniche, R. Gros-Bonnivard, P. Jaud, J. Valle-Marcos, J. M. Amann and C. Bouallou, *Appl Therm Eng*, 2010, **30**, 53-62.
10 B. J. P. Buhre, L. K. Elliott, C. D. Sheng, R. P. Gupta and T. F. Wall, *Prog Energ Combust*, 2005, **31**, 283-307.
11 Q. A. Wang, J. Z. Luo, Z. Y. Zhong and A. Borgna, *Energ Environ Sci*, 2011, **4**, 42-55.
12 P. Nugent, Y. Belmabkhout, S. D. Burd, A. J. Cairns, R. Luebke, K. Forrest, T. Pham, S. Q. Ma, B. Space, L. Wojtas, M. Eddaoudi and M. J. Zaworotko, *Nature*, 2013, **495**, 80-84.
13 Z. R. Herm, J. A. Swisher, B. Smit, R. Krishna and J. R. Long, *J Am Chem Soc*, 2011, **133**, 5664-5667.
14 J. Schell, N. Casas, R. Blom, A. I. Spjelkavik, A. Andersen, J. H. Cavka and M. Mazzotti, *Adsorption*, 2012, **18**, 213-227.
15 S. Cavenati, C. A. Grande and A. E. Rodrigues, *J Chem Eng Data*, 2004, **49**, 1095-1101.
16 D. Y. Zhao, J. L. Feng, Q. S. Huo, N. Melosh, G. H. Fredrickson, B. F. Chmelka and G. D. Stucky, *Science*, 1998, **279**, 548-552.
17 C. T. Kresge, M. E. Leonowicz, W. J. Roth, J. C. Vartuli and J. S. Beck, *Nature*, 1992, **359**, 710-712.
18 N. Stock and S. Biswas, *Chem Rev*, 2012, **112**, 933-969.
19 J. E. Park, H. K. Youn, S. T. Yang and W. S. Ahn, *Catal Today*, 2012, **190**, 15-22.
20 S. Schacht, Q. Huo, I. G. VoigtMartin, G. D. Stucky and F. Schuth, *Science*, 1996, **273**, 768-771.
21 Q. Huo, J. Feng, F. Schüth and G. D. Stucky, *Chem Mater*, 1997, **9**, 14-17.
22 T. Forster, S. Scholz, Y. Z. Zhu and J. A. Lercher, *Micropor Mesopor Mat*, 2011, **142**, 464-472.
23 S. Scholz, S. R. Bare, S. D. Kelly and J. A. Lercher, *Micropor Mesopor Mat*, 2011, **146**, 18-27.
24 S. Scholz, H. Shi and J. A. Lercher, *Top Catal*, 2012, **55**, 800-810.
25 S. Scholz and J. A. Lercher, *Chem Mater*, 2011, **23**, 2091-2099.
26 D. Y. Zhao, J. Y. Sun, Q. Z. Li and G. D. Stucky, *Chem Mater*, 2000, **12**, 275-279.
27 C. J. Brinker, *J. Non-Cryst. Solids*, 1988, **100**, 31-50.
28 H. D. Gesser and P. C. Goswami, *Chem Rev*, 1989, **89**, 765-788.
29 G. Kickelbick, *Prog. Polym. Sci.*, 2003, **28**, 83-114.
30 C. J. Brinker, D. M. Smith, R. Deshpande, P. M. Davis, S. Hietala, G. C. Frye, C. S. Ashley and R. A. Assink, *Catal Today*, 1992, **14**, 155-163.
31 C. J. Brinker and G. W. Scherer, *Sol-gel science: the physics and chemistry of sol-gel processing*, Academic Press, INC, San Diego, 1990.
32 D. H. Ripin and D. A. Evans, *pKa's of CH bonds at Heteroatom Substituted Carbon & References* 2014.
33 GESTIS, *Information system on hazardous substances of the German Social Accident Insurance*.
34 H. Pfeiffer, P. Bosch and S. Bulbulian, *Mater Chem Phys*, 2003, **78**, 558-561.
35 G. Busca and V. Lorenzelli, *Mater Chem*, 1982, **7**, 89-126.
36 M. Bensitel, V. Moravek, J. Lamotte, O. Saur and J. C. Lavalley, *Spectrochim Acta A*, 1987, **43**, 1487-1491.
37 K. Pokrovski, K. T. Jung and A. T. Bell, *Langmuir*, 2001, **17**, 4297-4303.
38 Z. Dang, B. G. Anderson, Y. Amenomiya and B. A. Morrow, *J Phys Chem-Us*, 1995, **99**, 14437-14443.
39 K. T. Jung and A. T. Bell, *J Catal*, 2001, **204**, 339-347.

40 R. W. Stevens, Jr., R. V. Siriwardane and J. Logan, *Energy & Fuels*, 2008, **22**, 3070-3079.
41 P. Linga, R. Kumar and P. Englezos, *J Hazard Mater*, 2007, **149**, 625-629.
42 D. Ko, R. Siriwardane and L. T. Biegler, *Ind Eng Chem Res*, 2003, **42**, 339-348.